JOURNAL OF PROPULSION AND POWER
Vol. 16, No. 5, September–October 2000

Unsteady Viscous Flow Causing Rotor–Stator Interaction in Turbines, Part 2: Simulation, Integrated Flowfield, and Interpretation

A. Chernobrovkin* and B. Lakshminarayana†
Pennsylvania State University, University Park, Pennsylvania 16802

Numerical simulation has been performed to investigate the unsteady flow physics associated with the nozzle–rotor wake interaction in turbines. A comparison between the predicted and the experimental unsteady pressure on the blade surface presented by Lakshminarayana et al. (Lakshminarayana, B., Chernobrovkin, A., and Ristic, D., "Unsteady Viscous Flow Causing Rotor-Stator Interaction in Turbines, Part 1: Data, Code Pressure," *Journal of Propulsion and Power*, Vol. 16, No. 5, 2000, pp. 744–750) shows good agreement. The predicted flowfield also correlates well with the blade-to-blade laser Doppler velocimetry data. Results of the numerical prediction in conjunction with the experimental data have been used to gain a better understanding of the unsteady flow physics. An assessment of the viscous and the inviscid contribution to the nozzle wake decay and the unsteady loss distribution in the rotor passage reveals the dominant effect of the viscous decay upstream of the leading edge. Inside the passage, the inviscid effects have a significant influence. The numerical solver has been able to predict most of the features associated with the unsteady transition on a turbine blade. The predicted flow at the off-design condition has been interpreted to understand the nature of the unsteady flowfield at a high negative incidence angle.

Nomenclature

C_f = skin friction coefficient, $\tau_w/(\rho_1 \bar{W}_1^2)$
C_p = pressure coefficient, $(p - \bar{p}_1)/(\rho_1 \bar{W}_1/2)$
C_x = axial chord length
i = incidence angle
k = turbulent kinetic energy
P_0 = total pressure in relative frame
p = static pressure
Re = Reynolds number based on chord
S = rotor blade spacing
S_1 = local passage width (rotor)
s = surface length from the leading edge
T = period
Tu = turbulence intensity based on inlet total relative velocity
Tu_r = unresolved unsteadiness
Tu_t = turbulence intensity based on local total relative velocity
t = physical time
U_m = rotational velocity at midspan
V = absolute total velocity
W = total relative velocity
x = axial length measured from rotor leading edge
y = distance in pitchwise direction
α = absolute flow angle
β = relative flow angle
ΔV = wake defect
ΔC_p = $C_p - C_{p_{\mathrm{av}}}$
ε = dissipation rate
ζ = loss coefficient, $= (\bar{P}_{01} - P_0)/(\rho \bar{W}_1^2/2)$
μ_t = eddy viscosity coefficient
ν = kinematic viscosity
τ = pseudotime
Ω = reduced frequency, $\omega C_x / V_{x0}$
ω = wake passing frequency

Subscripts

av = time average
dis = viscous dissipation
inv = inviscid
loc = local
max = maximum outside rotor wake
pot = pressure gust effect
str = inviscid stretching
t = turbulent
vis = viscous
wake = nozzle wake center
x = axial
δ = at the edge of the boundary layer
0 = inlet to the nozzle, freestream, reference point
1, inl = rotor inlet, time, mass average
2 = rotor outlet

Superscripts

$\sim$ = ensemble average
$'$ = unresolved unsteadiness
$-$ = time average

Introduction

A BRIEF description of the experimental facility, laser Doppler velocimetry (LDV) measurement of the flowfield, and the dynamic pressure on the blade at the midspan location is presented by Lakshminarayana et al.[1] Details of the Navier–Stokes code and the sensitivity study carried out to assess its accuracy in predicting the unsteady flow, including the transition, is also covered by Lakshminarayana et al. The objective of this paper is to provide an integrated interpretation of the data and the numerical prediction to understand the flow physics associated with the nozzle wake–rotor interaction. The velocity and pressure field is interpreted to derive information on the sources and effects of unsteady flow, the nozzle wake decay through the rotor passage, rotor–wake decay characteristics, and the unsteady transition on the blade. The approach followed in this paper is to examine both the surface properties and the flowfield within the passage to interpret the flow physics. In

---

Presented as Paper 98-3596 at the AIAA/ASME/SAE/ASEE 34th Joint Propulsion Conference, Cleveland, OH, 13–15 July 1998; received 14 August 1998; revision received 21 June 1999; accepted for publication 28 June 1999.

[*] Research Assistant, Center for Gas Turbines and Power. Member AIAA.

[†] Evan Pugh Professor, Director of Center for Gas Turbines and Power. AIAA Fellow.

addition, an attempt has been made to examine the losses associated with the unsteady flow. Additional simulations include the effect of inlet turbulence on the nozzle wake–blade interaction.

Unsteady Flowfield due to Rotor–Stator Interaction

A brief description of the data acquired from the LDV inside the passage at the midspan of the turbine rotor is given in Refs. 1 and 2. These data are compared with predictions in this section.

To enable a comparison of the measured rotor shaft phase-locked blade-to-blade flowfield with the numerical prediction, the data from the computation were processed in the same way as the experimental technique. The derived blade-to-blade distributions of the wake defect and the unresolved unsteadiness [Eq. (1), Ref. 1] in the absolute frame of reference are shown in Figs. 1 and 2, respectively. Note that the unresolved unsteadiness consists of both random fluctuations due to turbulence as well as fluctuations not associated with the rotor blade passing frequency. The velocity field is shown for the position $N1$ (Fig. 1, Ref. 1, bottom station), whereas the unresolved unsteadiness distribution is plotted for the position $N4$. Because of the blade shadow and lack of seeding, no experimental data are available in the unshaded (white) region. The velocity represents the periodic unsteadiness due to the nozzle wake $\tilde{V}$ [ensemble average minus the time average, Eq. (1), Ref. 1]. A comparison between the data and the prediction shows good agreement with the location and the defect in the nozzle wake. The numerical prediction moderately underpredicts the level of the wake defect between $x/C_x = 0$ and $x/C_x = 0.2$ (Fig. 2). The measured unresolved unsteadiness and the predicted turbulence intensity (Fig. 2) indicates that the peak intensities are predicted reasonably well, but the wake width based on the unsteadiness shows that the computation has a larger nozzle wake diffusion (into the freestream) compared with the experimental data.

Even though the rotor shaft phase-locked flowfield can be used to analyze the development of the unsteady flow in a rotor passage due to the wake–rotor interaction, it is more appropriate to consider the instantaneous flowfield. In this paper, rotor shaft phase-locked representation is used only to compare the measured velocity field with the numerical prediction. All subsequent discussion is based on the time accurate (instantaneous) flowfield.

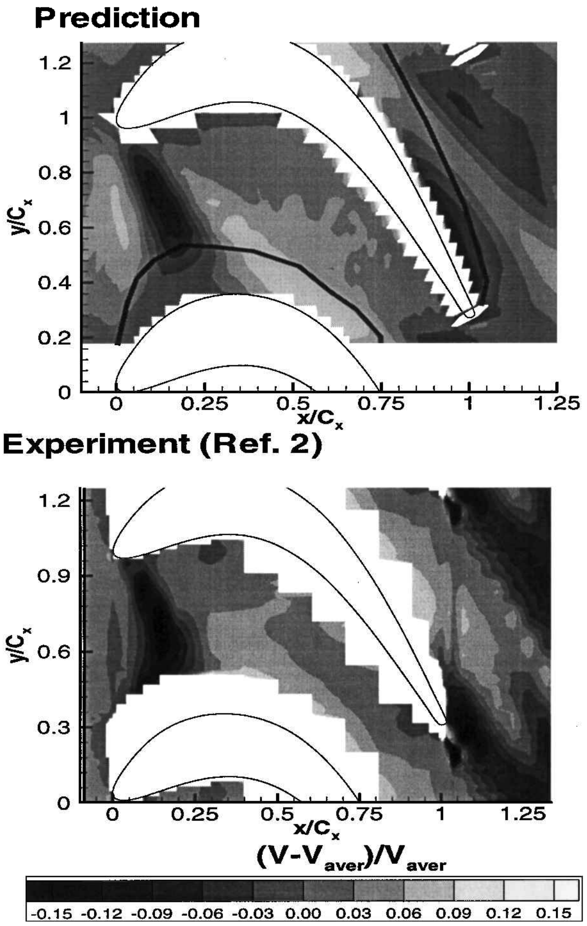

Fig. 1 Nozzle wake defect at the nozzle LDV position $N1$.

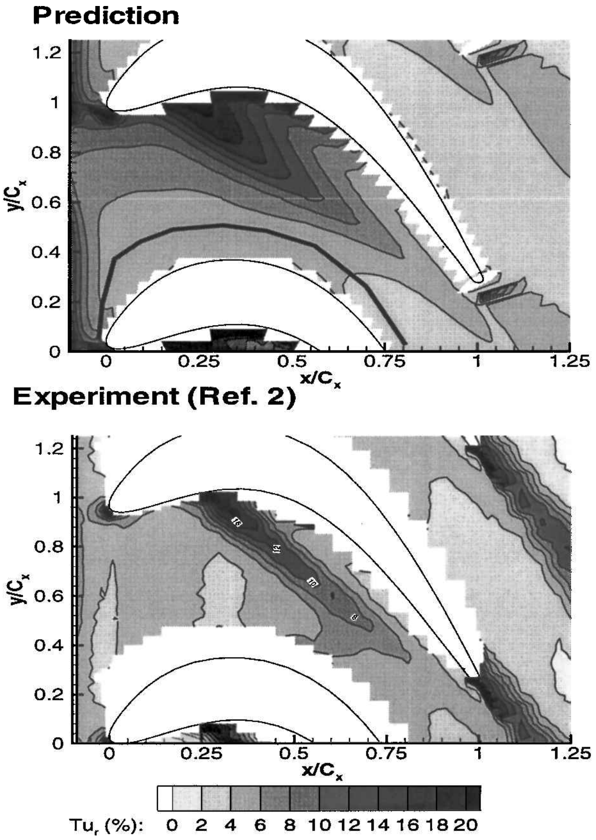

Fig. 2 Unresolved unsteadiness at nozzle LDV position $N4$.

Discussion of Unsteady Flow Physics

As indicated earlier, the vane–blade ratio used in the computation is 4:5; hence, the unsteady flowfield is computed in five rotor passages. Hence, all of the simulation data shown in this and subsequent sections show predictions in five rotor passages.

The unsteady velocity, pressure, and turbulence fields, shown in Figs. 3, 4, and 5, respectively, reveal the development of the rotor unsteady field caused by the nozzle wake–rotor interaction. Based on the unsteady velocity, the nozzle wake appears as a negative jet moving toward the suction side (Fig. 3). The nature of such impingement depends on the inlet velocity triangle and the wake defect. The location and propagation of the nozzle wake can be clearly identified by examining all of the instantaneous properties: unsteady velocity $(V - \bar{V})$, static and stagnation pressure, and turbulence field. The shape of the turbulence wake is very close to that of the entropy wake, which is normally used to identify the wake position. For the sake of brevity, the unsteady entropy distribution is not shown.

The wake segment is initially straight (Fig. 3). Because of the potential effect and the blockage caused by the leading edge, it is stretched, distorted, and diffused as it approaches the rotor leading edge. Farther downstream, the wake is chopped and transported at the local convection speed as a separate segment. Because of the large convection velocity near the suction side, spreading of the suction leg of the wake segment is much faster. When the wake segment reaches the trailing edge of the pressure surface, the wake is chopped on the suction side of the leading edge (Fig. 3).

As observed by other investigators, the wake propagation through a passage generates a system of counter-rotating vortices. Analysis of the unsteady flow shows two main sources of unsteady pressure on the blade surface. The interaction of counter-rotating vortices with the passage flow is the primary source of the unsteady pressure

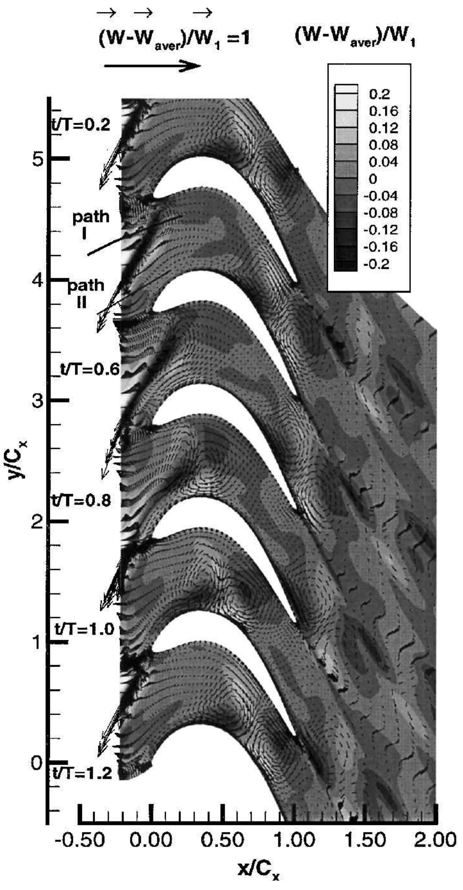

Fig. 3 Unsteady velocity field in the rotor passage.

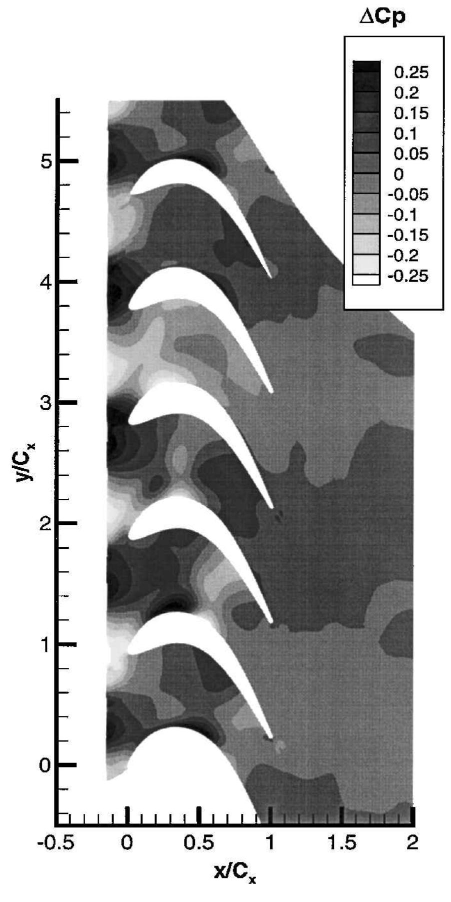

Fig. 4 Unsteady pressure field inside the rotor passage.

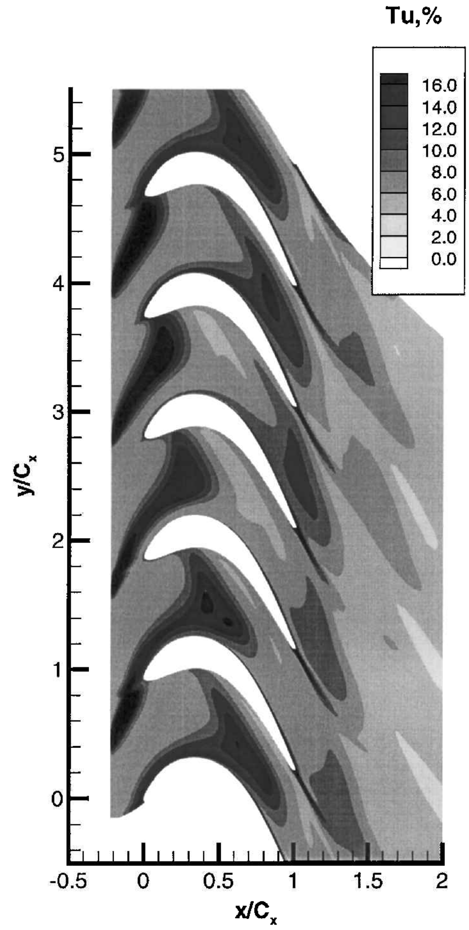

Fig. 5 Transport of the nozzle wake turbulence in the rotor passage.

field beyond 20% of the chord (Fig. 4). The second source is the interaction due to the pressure gust associated with the nozzle wake. A rapid decay of the inlet unsteady pressure field limits the influence of the pressure gust to the leading-edge region. The interaction of the pressure gust with the blade at the leading edge generates a zone of high pressure on the suction side (Fig. 4).

Additional simulations were carried out to investigate the contribution of the velocity gust and the pressure gust due to the nozzle wake and the rotor blade. In the first case, only the velocity defect is present; the second case has only the pressure gust. Distribution of the instantaneous velocity and pressure fields for these three inlet conditions are shown in Fig. 6. In the absence of the velocity defect, the pressure gust generates a system of counter-rotating vortices with rotation in a direction opposite to those induced by velocity gust. Near the leading edge, the variation in the surface pressure due to the velocity gust and the pressure gust has a phase angle variation of nearly 180 deg, as shown in Fig. 7, at $x/C_x = 0.71$. At this location, the pressure gust has a dominant effect. As a result, combined flow has only one peak related to the pressure gust. An interesting feature of the pressure gust–blade interaction is that it generates a significantly smaller pressure oscillation on the pressure side near the leading edge in comparison with the suction side. This can be explained by the shorter interaction time on the pressure side.

In the absence of the pressure gust, pressure oscillations are small within the initial 15% of the chord. The only significant effect of this interaction is the decreased skin-friction coefficient on the pressure surface. At moderately off-design flow conditions, this phenomenon may lead to an earlier development of the separation bubble due to the nozzle–wake blade interaction and may generate significant additional losses.

Beyond 20% of the chord, the pressure gust has a minimal impact on the unsteady pressure field on the suction surface (Fig. 8). Downstream of this location, the interaction between the nozzle wake-induced counter-rotating vortices develop a high-pressure

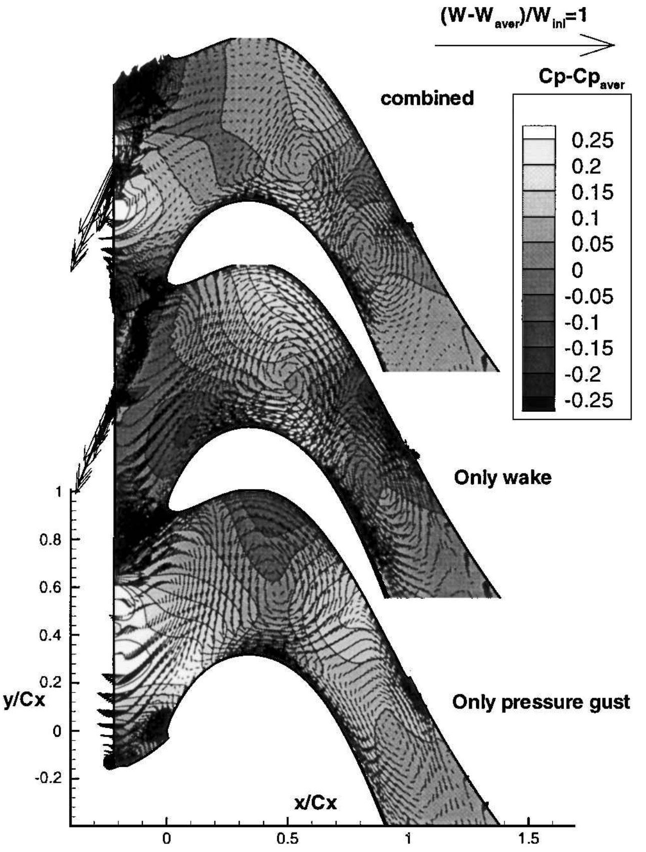

Fig. 6 Unsteady velocity and pressure field with different inlet boundary condition.

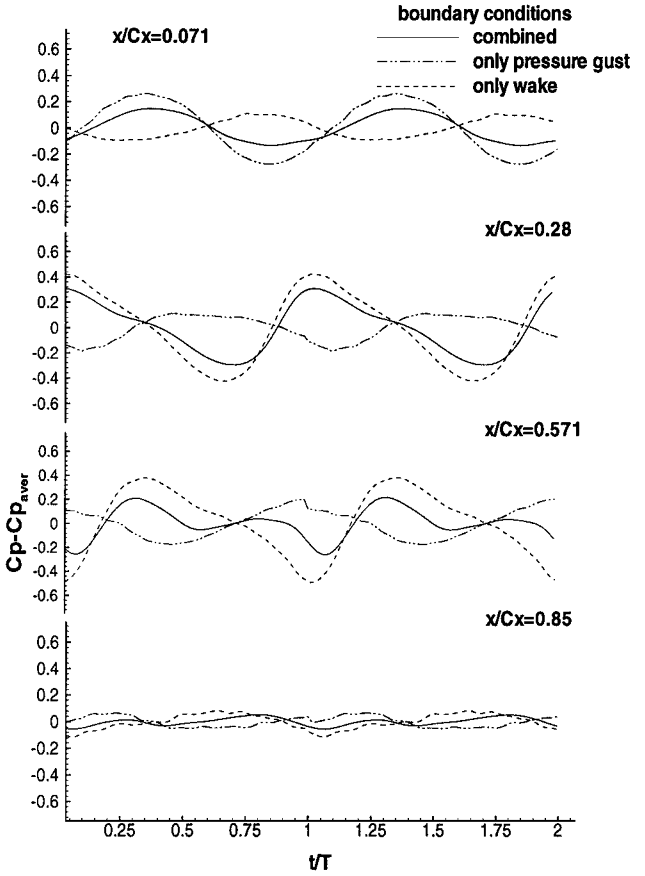

Fig. 7 Predicted time history of the surface pressure with different inlet boundary condition.

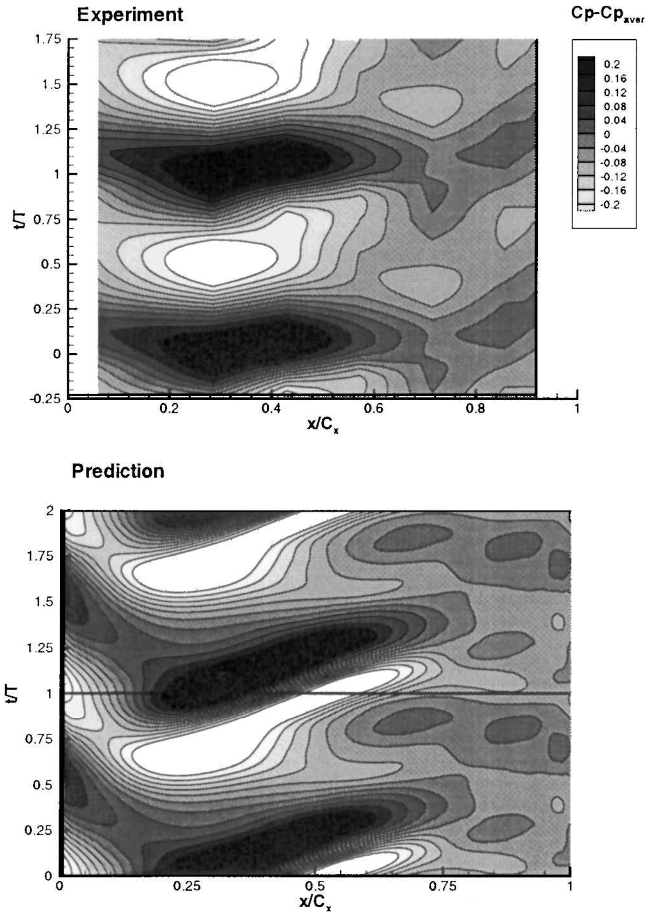

Fig. 8 Unsteady pressure coefficient, suction surface.

zone upstream of the nozzle wake center and a low-pressure zone downstream. This unsteady pressure system propagates downstream on the suction surface at the convection velocity, that is, velocity at the boundary-layer edge near the suction surface. The location of the maximum pressure is close to the location of the maximum wake defect. Downstream of $x/C_x = 0.7$, the unsteady pressure decays due to a decreased intensity of counter-rotating vortices.

Interaction between the passing wake and the pressure surface is significantly weaker because of a very small variation of the velocity field in the vicinity of the blade downstream of $x/C_x = 0.3\%$. The resulting amplitude of the unsteady pressure on the pressure surface is less than one-third of those at the suction surface.

The measured and predicted unsteady pressure coefficient on the suction surface at the design condition is shown in Fig. 8. Many of the features were described earlier.[1] The measurement does not show the effect of the pressure gust near the leading edge, because there are no data available at this location. However, the trend from 5–20% of the chord indicates that the distribution is similar to the predictions. The distribution beyond 20% of the chord shows the major influence of the velocity gust and the associated counter-rotating vortices. Predictions are in good agreement with the data. Both measurements and predictions indicate that unsteady pressures are negligible beyond about 70% of the chord.

Nozzle Wake Decay Through the Rotor Passage

The nozzle wake is a source of additional mixing losses in turbine passages. The physics of the wake mixing consists of two main components: viscous dissipation and inviscid effects (chopping, stretching, distortion, area changes, etc.). The wake decay due to the viscous dissipation results in losses, whereas the inviscid effects are the reversible process. In some cases, wake ingestion can be used to increase the efficiency of the propulsion system.[3]

Based on experimental and analytical investigations, Hill et al.[4] suggested a wake decay model in a diffusing flow that includes both the viscous and the inviscid effects. Van Zante et al.[5] developed an inviscid wake model for two-dimensional compressor blade row. This model estimates the inviscid decay of the wake defect as a function of the cascade flow parameters. The wake propagation in a turbine is more complex in nature when compared to that in a compressor. Because of a strong variation of the flow velocity in both the streamwise and the pitchwise directions, the wake is highly distorted and can not be considered as straight or slightly bent segments. To analyze the wake stretching in a turbine, it should be considered as a set of segments undergoing stretching/compression under significantly different local conditions.

An understanding of the viscous and inviscid contributions to the wake mixing is essential for minimization of the mixing losses. An analysis of the wake mixing based on the viscous and inviscid prediction is carried out to investigate the physics of the nozzle wake decay in a rotor passage. The three following cases are simulated: 1) base flow, viscous simulation (includes inviscid effect); 2) base flow, inviscid simulation; and 3) modified base flow, viscous simulation, no unsteady pressure variation at inlet. Case 3 is denoted as no pressure gust.

A comparison of the wake decay in the absolute frame of reference for all cases is shown in Fig. 9. At the trailing edge, the nozzle wake defect based on the inviscid prediction is three times larger than that predicted by the viscous simulation.

Viscous and inviscid predictions have a different wake decay rate inside the rotor passage, but a similar wake flow pattern exists at all locations. This enables a comparison between the inviscid and the viscous wake decay at different locations inside the rotor passage, even though the local wake defect is different in viscous and inviscid predictions. It is assumed (and verified through the numerical modeling) that at each particular location the inviscid rate of the wake decay is not a function of the local wake velocity defect. Thus, the inviscid contribution to the wake decay from the viscous solver can be compared with that based on the inviscid simulation despite the difference in an amplitude of the local wake defect.

Different mechanisms contribute to the wake decay and mixing in a rotor passage. There are significant variations in the viscous/inviscid effects at each axial location. It is possible to segregate the rotor passage into zones based on the characteristics of the nozzle wake decay. The boundaries of the various zones are shown in Table 1. The first zone extends from the inlet computational plane to $x/C_x = -10\%$ upstream of the leading edge. In this region, the nozzle wake is advanced as a set of parallel segments convected by the mean flow. The wake segment transported along path I (Fig. 3) undergoes stretching in the streamwise direction due to a 20% decrease in the streamwise velocity. This effect is clearly seen in Fig. 9 (line 2), in the form of the increased inviscid wake defect. A decrease in the inviscid wake defect beyond $x/C_x = -0.15$ is associated with the potential effect, which is described hereafter for the second zone. The wake segment traveling along path II (Fig. 3) undergoes an opposite process. Flow acceleration (40% increase in the local velocity) upstream of the suction surface results in a significant decrease in the wake defect (Fig. 9). The ratio of the maximum to minimum inviscid wake defect at $x/C_x = 0.1$ is equal to 1.45. Viscous dissipation has a more profound influence on the wake propagation along path I in comparison with path II.

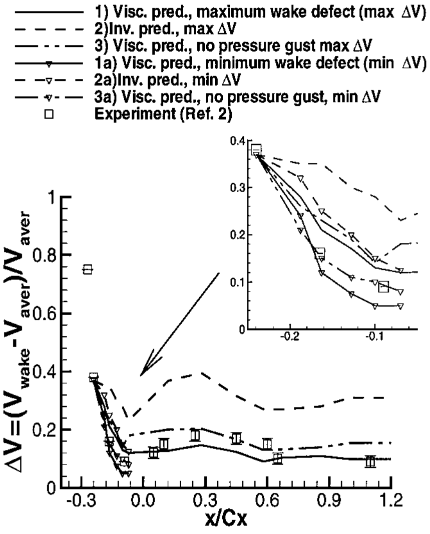

Fig. 9 Decay of nozzle wake defect.

Table 1 Zone boundaries

Zone number	Beginning x/C_x	End x/C_x
1	−0.24	−0.1
2	−0.1	0.05
3	0.05	0.25
4	0.25	0.6
5	0.6	Outlet

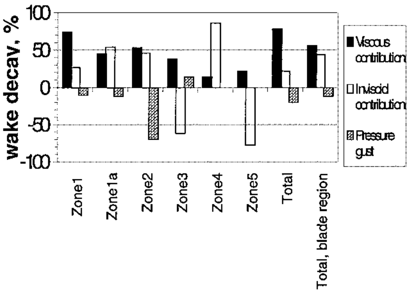

Fig. 10 Wake decay budget.

For each zone, the contribution of the viscous dissipation can be calculated:

For wake decay due to the viscous dissipation,

$$\delta\Delta V_{\text{dis}} = \delta\Delta V_{\text{vis}} - \delta\Delta V_{\text{inv}}$$

For change in the wake defect due to the inviscid effect,

$$\delta\Delta V_{\text{str}} = \delta\Delta V_{\text{inv}}$$

where $\Delta V = (V_{\text{wake}} - \bar{V})/\bar{V}$ is a local wake defect, $\delta\Delta V$ is the change in wake defect between the two axial locations, and subscripts inv and vis denote the inviscid and viscous solutions, respectively.

Viscous contributions to the wake mixing, presented in Fig. 10, are defined as follows:

$$\frac{\delta\Delta V_{\text{dis}}}{\delta\Delta V_{\text{dis}} + |\delta\Delta V_{\text{inv}}|}$$

and inviscid

$$\frac{\delta\Delta V_{\text{str}}}{\delta\Delta V_{\text{dis}} + |\delta\Delta V_{\text{inv}}|}$$

For zone $N \geq 2$, the predicted inviscid wake at the inlet to the zone is scaled by the predicted viscous wake defect at the current location, that is, $(\delta\Delta V_{\text{inv}})' = \delta\Delta V_{\text{inv}} \times (\Delta V_{\text{vis}}/\Delta V_{\text{inv}})$. Contributions of the potential effect are calculated as $\delta\Delta V_{\text{pot}} = (\delta\Delta V_{\text{visnopot}} - \delta\Delta V_{\text{vis}})/\delta\Delta V_{\text{vis}}$, where the subscript visnopot denotes case 3. A positive sign indicates that the pressure gust increases the wake decay. Similar to the preceding equations, the wake defect scaling is used to normalize the wake $\delta\Delta V_{\text{visnopot}}$.

The inviscid mixing is responsible for 30% of the total wake decay along path I (denoted as zone 1 in Fig. 10). For path II, intense stretching of the wake segment increases the inviscid contribution to about 50%. Downstream of $x/C_x = 0.1$, only the propagation of the maximum wake defect is considered.

The essential difference between the first and the second zone (from 10% upstream of the leading edge to 5% of the chord from the leading edge) is the increased contribution by the pressure gust. Viscous simulation, without the unsteady pressure field at the inlet

Table 2 Wake decay zones 4 and 5

Zone number	Predicted	Inviscid stretching (estimated)
4	0.64	0.68
5	1.08	1.20

(case 3) predicts a significant increase in the maximum wake defect over the baseline (case 3, Fig. 9). The comparison, shown in Fig. 6, can be used to interpret the influence of the moving pressure gust on the nozzle wake decay. This influence can be separated into two parts. The first effect is the generation of an additional favorable pressure gradient, resulting in enhanced mixing. At the inlet, the wake segment is located in the region of high pressure. When the wake is convected downstream, the region of high pressure is replaced with a zone of low pressure due to relative nozzle–rotor movement. A numerical simulation with no-wake boundary conditions reveals another contributing factor in increased wake decay due to the pressure gust. Even though no time-dependent velocity component was presented at the inlet, the moving pressure field generates the jet-wake structure shown schematically in Fig. 6. The jet, associated with the moving pressure field, is located above the nozzle wake. Thus, the velocity at this side of the wake is increasing, contributing to the decay of the wake defect. Counterclockwise rotation of the wake segment leads to a compression of the wake segment near the leading edge of the pressure side. This counterbalances the decay in the wake defect due to the pressure gust. The combination of these two effects results in a smaller net change in the inviscid decay of the wake defect. Overall, the contribution of the viscous and inviscid mechanisms is approximately equal in this region (Fig. 10).

In the third region (zone 3, Table 1), which extents from 5% of the chord up to 25% of the chord, the location of the maximum nozzle wake defect is moving rapidly from the pressure side to the suction side (Fig. 3). After the nozzle wake is chopped at the leading edge, two counter-rotating vortices develop in the rotor passage. At $x/C_x = 10\%$, the slip velocity vector (Figs. 1 and 3, Ref. 1) is pointed in the direction of the suction surface. Transport of a low-momentum fluid from the pressure surface to the suction side is the dominant mechanism responsible for the amplification of the wake defect in this region. The acceleration of the convection velocity in the direction of wake propagation leads to wake thickening and a further increase of the wake defect. A viscous dissipation contribution is only 60% of the inviscid one in this region (Fig. 10).

At $x/C_x = 30\%$ (Fig. 3), the wake is strongly bent with two legs extending from the suction to the pressure surface. A maximum wake defect is located on the suction side, closer to the wake center. The slip velocity is parallel to the streamwise direction. Further propagation of the wake segment containing a maximum wake defect can be considered through its rotation-free elongation–compression in the streamwise direction. Following the velocity field, the wake defect is decreasing from $x/C_x = 30$ to 60%. The wake defect increases from $x/C_x = 60$ to 100% because the streamwise total velocity decelerated by 13% (Fig. 9).

In both zones 4 and 5, the inviscid phenomenon is the major mechanism for the wake decay (Fig. 10) and is responsible for more than 70% of the changes in the wake defect. In zones 4 and 5, the wake decay can be estimated using the formula for inviscid stretching. The estimated values are as follows (Table 2): Within the blade passage, the inviscid stretching results in a net increase of the wake defect (Fig. 9, line 2). In summary, the viscous dissipation is responsible for 60% of the wake decay within the passage and for 75% from the inlet (upstream) to the trailing edge.

The data on the interaction of the nozzle wake with rotor wake are presented and interpreted in the preprint version of the paper (Ref. 6).

Loss Generation due to Unsteady Flow

The loss estimate is one of the most challenging tasks for computational fluid dynamicists. Numerical simulation based on different numerical solvers may result in an appreciable variation in the predicted losses (see, for example, Ref. 7). However, the prediction of the trend in losses is consistent. Based on a comparison between the predicted and measured flow characteristics presented in this paper, a certain level of confidence is achieved in the predicted loss distribution. However, the absolute level of the predicted loss should be verified through a comparison with measurements. An additional inviscid numerical simulation was carried out to assess the presence of the nonphysical losses due to the numerical errors (artificial dissipation, grid influence, etc.). A grid identical to those in the viscous solver was used to ensure consistency. It was found that the time mean (the pitchwise mass averaged) loss coefficient based on an inviscid calculation is found to be less than 0.01 or less than 4% of the maximum ζ at the outlet based on the viscous solver. This is an acceptable level of inaccuracy. The predicted flow and the pressure field can be used to analyze the distribution of losses through the passage, as well as additional losses due to the presence of the nozzle wake.

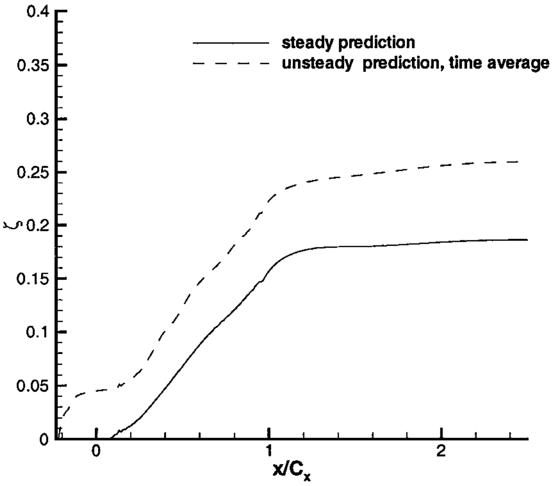

Fig. 11 Mass average loss coefficient.

The pitchwise averaged loss coefficient, shown in Fig. 11, can be used to identify sources of increased losses due to unsteady flow. The loss coefficient with unsteady flow is based on the unsteady inlet total pressure. Thus, it includes only losses in the rotor passage. There is a sharp increase in ζ upstream of the leading edge, an indication of the intense mixing in this region. This contribution accounts for 55% of the increased total loss coefficient in comparison with those based on the steady flow prediction. This loss can be represented as a loss due to the nozzle wake dissipation in the absence of the rotor–stator interaction and its modification due to the presence of the rotor. Comparison of the predicted losses upstream of the leading-edge location with and without a rotor shows that the differences is below the accuracy threshold. Therefore, no attempt was made to make a quantitative estimate of the rotor–stator interaction contribution to the loss distribution upstream of the rotor leading edge. Additional losses within the blade passage contribute 35% to the total unsteady losses. The steady and unsteady loss distribution is practically parallel from 25 to 50% of the chord. Thus, the profile losses due to the rotor boundary layer are dominant in comparison to the mixing losses due to the nozzle wake decay within the passage. The time-averaged boundary-layer properties reveal higher values of suction surface momentum thickness in comparison with the steady flow prediction beyond $x/C_x = 0.4$. This correlates well with the differences in ζ based on the steady and the unsteady flow prediction. There is a moderate increase ($\zeta \sim 0.07$) in the loss coefficient downstream of the trailing edge. This may be attributed to the nozzle wake–rotor wake interaction. However, this level of ζ increase is too small to be considered reliable.

Unsteady Transitional Flow on the Suction Surface

An accurate prediction of the unsteady transitional flow is crucial in evaluating losses, efficiency, and cooling requirements of

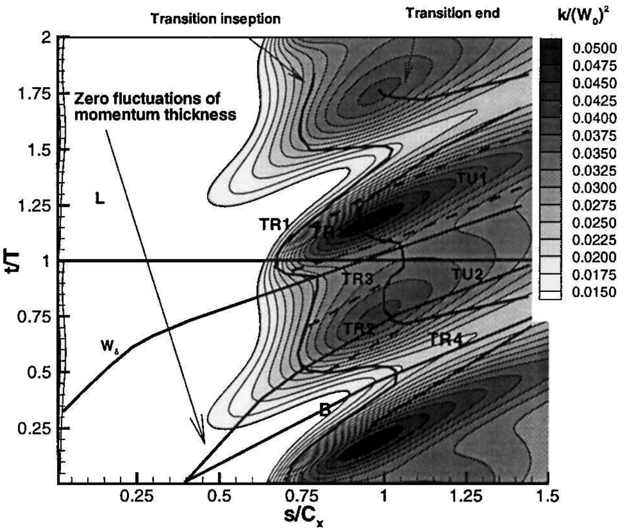

Fig. 12 Maximum turbulence kinetic energy in the boundary layer, suction surface.

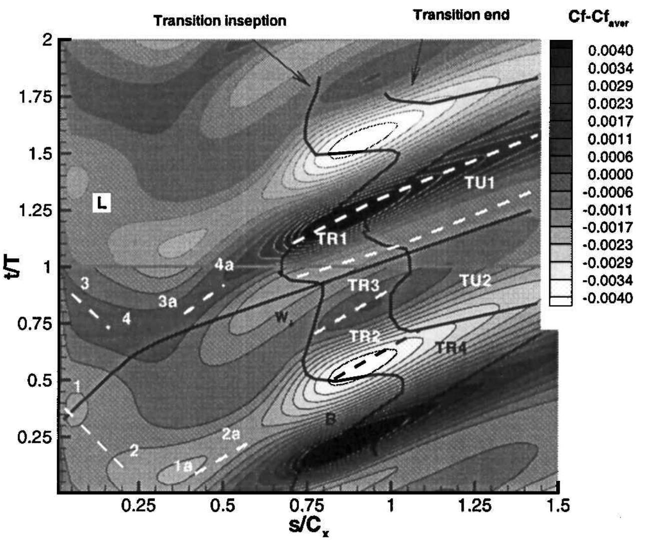

Fig. 13 Unsteady skin-friction coefficient, suction surface.

turbines. Very few attempts have been made to predict the unsteady transitional boundary layer on a turbine blade using the full Navier–Stokes solver.

A major feature of the unsteady flow in the present turbine rotor is the location of the maximum unsteadiness in the surface pressure, which is close to $x/C_x = 0.3$ ($s/C_x = 0.45$) (Fig. 8). This is close to the location of the transition onset; thus, the flow in the transition region is significantly affected. An accurate prediction of the pressure field is crucial to the prediction of the unsteady transitional zone.

Space–time distribution of the unsteady turbulence field, due to the interaction of the nozzle wake with blade surface boundary layer, is shown in Fig. 12. Here, the $t/T = 0$ line corresponds to the flow conditions in Fig. 3. Various zones in the unsteady boundary layer can be classified as follows (shown in Figs. 12 and 13): L is laminar region, TR1 wake-induced transitional strip, TU1 wake-induced turbulent strip, TR3 transition between wakes, TR2 wake turbulence-induced transition between wakes, TU2 turbulent flow between wakes, and TR4 transitional strip behind passing wake.

The unsteady nature of the transitional process makes it difficult to identify the beginning and the end of the transition. For steady flow simulation, the identification of the inception and the end of the transition can be based on the local turbulence field and verified through an analysis of the other flow characteristics, that is, skin-friction coefficient, shape factor, etc. It is found that this approach cannot be used in an unsteady flow due to a phase lag between different flow variables and properties in the transitional region. Hence, the location of the onset and the end of the transition is based only on the predicted turbulence field. The position of the transition inception is calculated as the position where $F(\mu_t^m)$ reaches its maximum value along the path on a space–time diagram (Fig. 12). $F(\mu_t^m)$ is the first derivative of μ_t^m along the wake path at the boundary-layer edge, and μ_t^m is the maximum value of the eddy viscosity inside the blade boundary layer at any given space–time position. The location of the maximum value of k at the end of the transitional zone was chosen as the location of the end transition. This criteria correlates well with the predicted value of the local maximum skin-friction coefficient.

The variation of the predicted unsteady skin-friction coefficient on the suction surface is shown in Fig. 13. As indicated earlier, from $x/C_x = 0$ to 0.25 the pressure gust is the primary source of unsteady pressure in the blade (Fig. 8). Beyond $x/C_x = 0.2$, the wake defect and the counter-rotating vortex system generate a combination of high-pressure and low-pressure zones that are convected in the streamwise direction. In the laminar region, the surface pressure variation is the primary source of boundary-layer disturbance. The observed variation of skin-friction coefficient along path 1–2 and 1a–2a, as well as 3–4 and 3a–4a, shown in Fig. 13, can be explained on the basis of an unsteady pressure gradient (favorable and adverse) at these locations (Fig. 8).

Near $x/C_x = 0.3$ ($s/C_x = 0.45$) interaction of the blade boundary layer with the nozzle wake increases the velocity at the boundary-layer edge (Fig. 3). At this location (Figs. 8 and 12), the Reynolds number, based on the momentum thickness (Re_θ), is 12% higher over the time-averaged value, reaching a value of $Re_\theta = 230$. The boundary-layer development along this path (going through point 1 in Fig. 13) undergoes wake-induced transition at $s/C_x = 0.68$. Transition within the wake-induced transitional strip TR1 is characterized by a maximum increase in the turbulence kinetic energy, as well as the maximum value of the unsteady skin-friction coefficient. After the boundary layer becomes fully turbulent, the nozzle wake disturbance leads to a wake-induced turbulent strip TU1. The transformation of the kinetic energy of the velocity fluctuation into the turbulence kinetic energy generates an increased level of k across the boundary layer in comparison with the zone of turbulent flow between wakes TU2. Declining pressure fluctuations and wake defect decay are the reasons for the vanishing shear stress fluctuations in the wake-induced strip beyond 80% of the chord.

Laminar flow in the region following the wake has a moderately decreased level of $Re_\theta = 200$ at 30% of the chord (this location corresponds to point 2, Fig. 13). The boundary-layer development behind the nozzle wake is characterized by a significantly delayed transition inception that occurs at $s/C_x = 0.98$ (TR4). Flow remains transitional up to the trailing edge. Unlike the wake-induced transition strip or the transition region between wakes, the turbulent kinetic energy does not undergo a rapid increase in the transition region, but rather further relaxation to the level of that in the developed turbulent boundary layer. The turbulent kinetic energy increases monotonically, rising from a low laminar value to one corresponding to those in the end of the transitional zone. An analysis of the boundary-layer development in this region leads to the conclusion that the diffusion of the turbulence kinetic energy between the freestream and the turbulent zones upstream and downstream is the primary mechanism responsible for the amplification in k.

The zone in between the passing wakes is not subject to an additional pressure gradient or other disturbance associated with the wake–blade interaction. Nevertheless, there is an earlier transition inception near $s/C_x = 0.70$ and $t/T = 0.5$. A comparison of the turbulent kinetic energy in the boundary layer (Fig. 12) and the blade-to-blade turbulence field (Fig. 5) shows an elevated level of turbulence in the boundary layer due to the maximum diffusion of the nozzle wake turbulence at this location. In the absence of the velocity disturbance, this high-turbulence level (about 5% increase in Tu_t) is the primary source of earlier transition in zone

TR2. A numerical simulation with no turbulence fluctuation in the nozzle wake confirmed this hypothesis. If there is no elevated level of turbulence in the nozzle wake, zone TR2 moves upstream and closer to zone TR1, merging with zone TR3 (transition between wakes). The boundary layer in zone TR2 has a lower increase in the momentum thickness and has a lower level of eddy viscosity. Thus, losses in this region are lower in comparison to those at the wake-induced transition/turbulent strips, but a little higher than that in the region of pure transition between wakes (zone TR3).

The flow in the Pennsylvania State University turbine has a high level of freestream turbulence. For this type of flow, the transition occurs through the bypass mechanism. The transition inception occurs at the location where an outer disturbance causes generation and growth of turbulent spots. The length of the transitional region depends on the spots' spreading angle and their growth. These characteristics are functions of a number of parameters: local momentum thickness, pressure gradient, Mach number, etc. At zero pressure gradient, the leading edge of the turbulent spot propagates at $0.88W_\delta$ (where W_δ is the wake propagation velocity at the edge of the boundary layer), whereas the trailing edge has propagation velocity equal to $0.5W_\delta$. The low Reynolds number $k-\varepsilon$ model, originally developed for the fully turbulent flow, models the transitional process through the diffusion of the freestream turbulence and a local balance between the turbulence production and the dissipation rate, which depend on the distribution of the velocity in the boundary layer. The unsteady flow results in unsteady transition on a blade surface. Disturbances, caused by the passing wake, lead to an earlier generation of the turbulent spots, which may form a turbulent strip. Turbulent spot growth and propagation mechanisms are essentially the same as in the case of the steady transition. The propagation velocity of the leading and the trailing edge of the wake-induced turbulent strips are equal to those of the turbulent spot, that is, $0.88W_\delta$ and $0.5W_\delta$, correspondingly. This is confirmed by the measurement (see, for example, Ref. 8). Development of the calmed region that is located behind the wake-induced transitional/turbulent strips, is another crucial element in the unsteady transitional process. The trailing edge of the calmed region propagates at $0.3W_\delta$. This region has laminar characteristics, but has an elevated level of shear stresses. This can be considered the relaxation zone between the turbulent and the laminar zones. Higher resistance to the separation and low boundary-layer losses associated with a calmed region are beneficial.

The low Reynolds number $k-\varepsilon$ model lacks the physics associated with the turbulence spot development and can model the transition process only in a global fashion. In the numerical prediction, the unsteady velocity fluctuation caused by the wake–blade interaction is the primary source of the earlier transition. The maximum value of the average turbulence kinetic energy and the maximum value of the k fluctuation across the boundary layer occur at the same location. After the transition inception, two major mechanisms are responsible for the further development of the predicted transitional strip. The first mechanism is the convection of the transitional zone at the local propagation speed, which is smaller than the wake propagation speed W_δ at the boundary edge. The second mechanism is the advection of the velocity disturbance with variable velocity across the boundary layer. It was found that the propagation speed of the transitional strip TR1, defined as a path along maximum k in Fig. 12, is equal to $0.66W_\delta$. This is higher than the propagation velocity equal to $0.55W_\delta$ at the location of the maximum turbulent kinetic energy across the boundary layer. Investigation of the time–space distribution of the velocity and turbulence across the boundary layers reveals that this increase is due to a greater speed of the velocity disturbance propagation, the second contributor to the development of the unsteady transitional zone. From Figs. 12 and 13, the leading-edge velocity of the transitional strip is estimated to be $0.9–1.0W_\delta$, whereas the trailing-edge velocity is about $0.5–0.55W_\delta$. As stated earlier, the transition in zone TR2 is due to an elevated level of freestream turbulence that is convected at the local propagation speed. Therefore, the propagation speed of the transition strip is equal to the local convection velocity inside the boundary layer ($0.55W_\delta$).

Zone B (Figs. 12 and 13) has several features of the calmed region. A low level of turbulent kinetic energy and eddy viscosity in this region is similar to that observed in a laminar flow. At the same time, it has an elevated level of shear stresses in comparison with the shear stress in the laminar zone. Phase lag between the maximum amplitude of k and the maximum amplitude of C_f at the transition inception (about 5% of t/T, Figs. 12 and 13) results in higher shear stresses in the zone above the wake-induced transitional strip. This phase lag diminishes farther downstream and is equal to zero at the end of the transition. There is a significantly delayed transition onset in zone B. A low level of the momentum thickness in combination with low eddy viscosity results in significantly smaller boundary-layer losses. Nevertheless, this region lacks another crucial feature of the calmed region. A predicted shear stress profile does not have relaxing distribution of C_f at the side of the calmed region. Experimental data indicate that the trailing edge of the calmed region is propagating at $0.3W_\delta$. In the prediction, the line of a zero momentum thickness variation, which can be considered as a boundary of the region B, has a propagation velocity equal to 47% of W_δ.

Effect of Inlet Turbulence

Additional simulation studies were carried out with different freestream turbulence intensities at the inlet. The design condition had a 7% turbulence intensity in the freestream at the inlet. The additional simulation includes freestream turbulence intensity of 2 and 15%, which is closer to that which exists in aircraft engines. The major feature is the decay of the nozzle wake. The amplitude of unsteady pressure distribution shown in Fig. 14 reveals that the freestream turbulence intensity plays a major role. The wake decay is slower and unsteadiness is higher at low turbulence intensity and decreases significantly as the turbulence intensity is increased

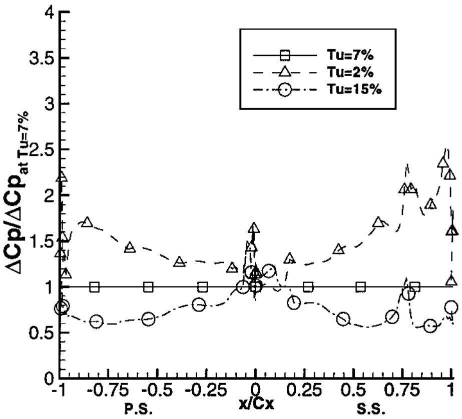

Fig. 14 Variation of the maximum blade unsteady pressure at different inlet turbulence levels.

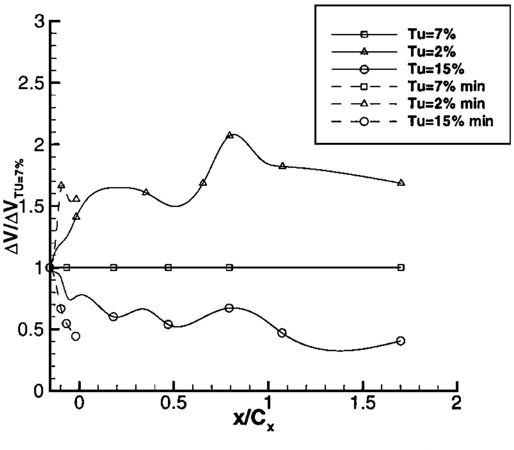

Fig. 15 Variation of the maximum wake defect [$\Delta V = (V_{\rm wake} - V_{\rm aver})/V_{\rm aver}$] at different inlet turbulence levels.

to 15%. This is confirmed by the nozzle wake defect plotted in Fig. 15.

Conclusions

The unsteady flow in a turbine rotor due to nozzle wake–rotor interaction is investigated numerically. The predicted velocity and pressure field is in good agreement with the experimental data at the design and the off-design conditions.

The pressure gust has the most influence near the leading edge. Beyond this, the counter-rotating vortices are the source of unsteadiness. The maximum variation in the unsteady pressure was observed at $x/C_x = 0.28$ on the suction surface.

Up to 15% of the chord, the viscous dissipation is responsible for 45–75% of the wake decay. Farther downstream, the wake undergoes both the inviscid decay and the amplification inside the passage. Because of the viscous dissipation, the contribution is equal to 75% of the total decay and 58% in the passage. Most of additional losses due to unsteady flow occur upstream of the leading edge (~55%). Inside the blade passage, the nozzle wake mixing losses are small in comparison with blade profile losses. The increase in profile losses is attributed to the modification of the suction surface boundary layer due to the nozzle wake–blade interaction.

The numerical solver was able to predict most of the features associated with the wake-induced unsteady transition (wake-induced transitional strip, turbulent strip, etc.). Even though the $k-\varepsilon$ model lacks the physics of the bypass transition, the predicted development of various zones follows the trend observed in the experiment. The major exception is the calmed region. The predicted region downstream of the wake-induced transitional strip possesses some characteristics of the calmed region. However, this region can not be identified as a calmed region because it lacks other essential features of the calmed region, such as the spreading angle of the zone with trailing edge propagating at $0.3W_\delta$.

The nozzle wake interaction with the rotor wake leads to an increased unsteadiness observed in both the experiment and the prediction. The suction side segment of the nozzle wake merges with the rotor wake, causing fluctuations in the rotor wake.

Acknowledgments

The experimental work was supported by NASA through NAG3-736, with R. Boyle and C. Civinskas serving as Technical Monitors, and the computational effort was partially supported by NASA Grant NAG3-2025, with D. Ashpis serving as Technical Monitor.

References

[1] Lakshminarayana, B., Chernobrovkin, A., and Ristic, D., "Unsteady Viscous Flow Causing Rotor-Stator Interaction in Turbines, Part 1: Data, Code Pressure," *Journal of Propulsion and Power*, Vol. 16, No. 5, 2000, pp. 744–750.

[2] Zaccaria, M., and Lakshminarayana, B., "Unsteady Flow Field due to the Nozzle Wake Interaction with the Rotor in Axial Turbine, Parts 1 and 2," *Journal of Turbomachinery*, Vol. 119, No. 2, 1997, pp. 201–224.

[3] Smith, L. H., Jr., "Wake Ingestion Propulsion Benefit," *Journal of Propulsion and Power*, Vol. 9, No. 1, 1993, pp. 74–82.

[4] Hill, P. G., Schaub, U. W., and Senoo, Y., "Turbulent Wakes in Pressure Gradients," *Journal of Applied Mechanics*, Dec. 1963, pp. 518–524.

[5] Van Zante, D., Adamczyk, J., Strazisar, A., and Okiishi, T., "Wake Recovery Performance Benefit in a High-Speed Axial Compressor," American Society of Mechanical Engineers, Paper 97-GT-535, June 1997.

[6] Chernobrovkin, A., and Lakshminarayana, B., "Experimental and Numerical Study of Unsteady Viscous Flow due to Rotor–Stator Interaction in Turbines, Part 2: Simulation, Integrated Flowfield & Interpretation," AIAA Paper 98-3596, July 1998, pp. 1–16.

[7] Venable, B. L., Delaney, R. A., Busby, J. A., Davis, R. L., Dorney, D. J., Dunn, M. G., Haldeman, C. W., and Abhari, R. S., "Influence of Vane Blade Spacing on Transonic Turbine Stage Aerodynamics, Part 1: Time-Averaged Data and Analysis," American Society of Mechanical Engineers, Paper 98-GT-481, June 1998.

[8] Halstead, D. E., Wisler, D. C., Okiishi, T. H., Walker, G. J., Hodson, H. P., and Shin, H.-W., "Boundary Layer Development in Axial Compressors and Turbines," American Society of Mechanical Engineers, Journal of Turbomachinery, Vol. 119, Nos. 1 and 2, pp. 114–139, 225–237.